



Numerical simulation of high Schmidt number flow over a droplet by using moving unstructured mesh

Rho-Taek Jung ¹, Toru Sato *

Department of Environmental and Ocean Engineering, University of Tokyo, 7-3-1 Hongo, Bunkyo-ku, Tokyo 113-8656, Japan

Received 2 December 2003; received in revised form 5 July 2004; accepted 23 August 2004
Available online 23 September 2004

Abstract

A direct numerical simulation code for flow over a droplet, which rises freely, deforms in shape, and dissolves into a continuous phase, was developed. A two-phase flow field was discretised by a cell-centred arbitrary Lagrangian–Eulerian finite volume formulation by using three-dimensional hybrid unstructured meshes, which consist of triangular prisms near interface for the resolution of viscous boundary layer and tetrahedrons in the other part. Since mass boundary layer is much thinner than that of momentum for high Schmidt number problems, very-thin-layer cells are generated within one layer of the prisms attached to the interface only for solving mass transfer. This can be claimed as a novelty of the present simulation method. From the simulation results, the mechanisms of shape deformation and/or oscillation, trajectory morphology, and vortex shedding are elucidated and correlated to mass transfer at moderately high Reynolds number.

© 2004 Elsevier Inc. All rights reserved.

Keywords: Two-phase flow; Direct numerical simulation; Moving unstructured mesh; Droplet deformation and shape oscillation; High Schmidt number

1. Introduction

Droplet flows with mass transfer are very important in industrial applications. There are also numerous problems about the dynamics of moving interfaces in two-phase flows, such as oil tank sloshing, capillary and density current flow, and atomising droplet jets. Numerical methods for predicting inter-

* Corresponding author. Tel.: +81 3 5841 6521; fax: +81 3 5802 3374.

E-mail address: sato-t@k.u-tokyo.ac.jp (T. Sato).

¹ Present address: Marine Safety and Pollution Control Lab., KORDI/KRISO, Yuseong, P.O. Box 23, Daejeon 305-600, Republic of Korea. Tel.: +82 42 868 7215; fax: +82 42 868 7738.

face positions are categorised into two main approaches, i.e., front-capturing and front-tracking methods. In the former approach, the location of interface is marked by a scalar-indicator function. Cell-wise segments are reconstructed by this scalar function to form interfaces at every time step of the computation. As the scalar function, we have the volume of fluid (VOF) [1], the marker density function (MDF) [2], and the level set method [3]. Sato et al. [4] simulated a droplet with mass dissolution from its interface by solving a transport equation of the MDF in orthogonal grids. Puckett et al. [5] addressed a drawback of the front-capturing, namely, how to ensure the preservation of the clear interface position and of the accurate conservation of mass. There have been several attempts to overcome this problem, such as Chang et al. [6] by coupling the level set formulation to the flow-governing equation and by extending the level set function to introduce its re-initialisation, Sussman et al. [7] by imposing a new constraint for improving the accuracy of the interface thickness, Raad et al. [8] by using adaptive fine grid resolution called “micro cells” near the interface in their rectangular grids, Ubbink and Issa [9] by adaptive combination of high resolution discretisation schemes in unstructured mesh, and Tomiyama et al. [10] by the cubic-interpolated propagation (CIP) scheme for the transport of the volume fraction in micro regular cells.

In the front-tracking method, the interface is tracked explicitly by marker particles in a Lagrangian way. The historical free-surface tracking technique was developed by Harlow and Welch [11], which is called the marker-and-cell (MAC) method and has led to many applications in various engineering fields. Unverdi and Tryggvason [12] and Tryggvason et al. [13] developed a front-tracking method for bubble/droplet flows, in which the interface is expressed by unstructured surface mesh connecting the marker particles. Agresar et al. [14] modified the two-dimensional version of this method in adaptive refined grids near the interface. Sato and Richardson [15] simulated two-dimensional moving fronts of a polymeric liquid by generating fringe finite-elements in the mesh that contains a front segment. Interestingly, Enright et al. [16] invented the particle level set method by the hybrid of front-capturing and front-tracking methods to rebuild the level set by the marker particles in poorly resolved regions. Merit and demerit of the methods are the avoidance of numerical diffusion in identifying interface position and the difficulties in coping with merging and breaking-up of the fluid mass, respectively.

At the region where the Schmidt number is greater than unity, mass boundary layer becomes thinner than that of momentum. For high Schmidt number problems about a droplet, even the methods with fine cells generated near the interface, such as [8–10,14,15], have a limitation in resolving the thin boundary layer. It seems that interface-fitted grids with the arbitrary Lagrangian–Eulerian (ALE) description, which are categorised in the front-tracking method, is the only way for this purpose, because the large gradient of mass concentration near the interface is efficiently resolved by adjusting the size of interface-fitted meshes, though such grids can hardly follow large deformation. For the interface-fitted grid system, we have had many applications so far. Miyata et al. [17] adopted structured free-surface-fitted grids to express three-dimensional nonlinear waves. Ryskin and Leal [18] and Takagi et al. [19] simulated a single rising bubble in axisymmetric and three-dimensional coordinates, respectively, by using structured boundary-fitted grids. Popinet and Zaleski [20] also solved three-dimensional bubble flows, where special attention is laid on the accurate calculation of surface tension. Braess and Wriggers [21] simulated free surface behaviour by two-dimensional triangle finite-elements.

In this study, a direct numerical simulation code was developed to solve flow over a moving and dissolving droplet by using three-dimensional hybrid unstructured meshes. The mesh system consists of triangular prisms near the interface for the resolution of viscous boundary layer and tetrahedrons in the other part. The interface between the droplet and the continuous phase moves in the way satisfying both kinematic and dynamic conditions. The two-phase flow field is discretised by a cell-centred ALE finite volume formulation, utilising the Rhie–Chow’s algorithm [22]. To resolve mass boundary layer thinner than the momentum boundary layer, we regenerated several additional computational cells named the very thin layers (VTLs) within one prism layer attached to the interface. The VTLs are used only to solve the mass transfer. The

objective of this paper is, by this numerical method, to elucidate the correlation mechanism between the droplet motion and the mass transfer rate at the interface.

2. Numerical procedure

2.1. The governing equations of two-phase flow

This study focuses on a liquid–liquid two-phase system, i.e., the continuous and dispersed phases, under gravitational fields. The governing equations for this system are the dimensionless continuity equation for the both phases and the dimensionless Navier–Stokes (NS) equation for each phase with the ALE description.

$$\nabla \cdot \mathbf{u} = 0 \quad \text{in } \Omega_c \text{ and } \Omega_d, \tag{1}$$

$$\frac{\partial \mathbf{u}}{\partial t} + \nabla \cdot (\mathbf{u} - \mathbf{v})\mathbf{u} = -\nabla \phi + \frac{1}{Re} \nabla [\nabla \mathbf{u} + (\nabla \mathbf{u})^T] \quad \text{in } \Omega_c, \tag{2}$$

$$\frac{\partial \mathbf{u}}{\partial t} + \nabla \cdot (\mathbf{u} - \mathbf{v})\mathbf{u} = -\frac{1}{\gamma} \nabla \phi + \frac{1}{Re} \frac{\theta}{\gamma} \nabla [\nabla \mathbf{u} + (\nabla \mathbf{u})^T] + \frac{1}{\gamma} \frac{Eo}{(OhRe)^2} \mathbf{g} \quad \text{in } \Omega_d, \tag{3}$$

where Ω is the considered three-dimensional region, \mathbf{u} is the flow velocity, \mathbf{v} is the velocity of coordinates that move, \mathbf{g} is the unit gravitational acceleration vector, $(0, 0, -1)$ in the Cartesian coordinate system, and ϕ is the modified pressure that excludes the hydrostatic pressure of the continuous phase. Re is the Reynolds number, Oh is the Ohnesorge number, Eo is the Eötvös number, and γ and θ are the density and the viscosity ratios, respectively, of the dispersion phase to the continuous phase. These dimensionless parameters are defined by

$$\gamma = \frac{\rho_d}{\rho_c}, \quad \theta = \frac{\mu_d}{\mu_c}, \quad Re = \frac{\rho_c U d_0}{\mu_c}, \quad Eo = -\frac{g(\rho_d - \rho_c)d_0^2}{\sigma}, \quad Oh = \frac{\mu_c}{\sqrt{\rho_c d_0 \sigma}}, \tag{4}$$

where ρ and μ are the density and the viscosity, respectively, d_0 is the diameter of the initial spherical droplet, U is the reference velocity, and σ is the interface tension. The subscripts c and d denote the values of the continuous and the dispersed phases, respectively.

The integral form of the dimensionless mass equation in the both phases and the dimensionless momentum conservation equations in each phase are:

$$\int_{\Gamma} \mathbf{u} \cdot \mathbf{n} \, dA = 0 \quad \text{in } \Omega_c \text{ and } \Omega_d, \tag{5}$$

$$\int_{\Omega} \frac{\partial \mathbf{u}}{\partial t} \, dV + \int_{\Gamma} \mathbf{u}(\mathbf{u} - \mathbf{v}) \cdot \mathbf{n} \, dA = - \int_{\Gamma} \phi \mathbf{n} \, dA + \frac{1}{Re} \int_{\Gamma} [\nabla \mathbf{u} + (\nabla \mathbf{u})^T] \cdot \mathbf{n} \, dA \quad \text{in } \Omega_c, \tag{6}$$

$$\begin{aligned} \int_{\Omega} \frac{\partial \mathbf{u}}{\partial t} \, dV + \int_{\Gamma} \mathbf{u}(\mathbf{u} - \mathbf{v}) \cdot \mathbf{n} \, dA = & -\frac{1}{\gamma} \int_{\Gamma} \phi \mathbf{n} \, dA + \frac{\theta}{\gamma} \frac{1}{Re} \int_{\Gamma} [\nabla \mathbf{u} + (\nabla \mathbf{u})^T] \cdot \mathbf{n} \, dA \\ & + \frac{1}{\gamma} \frac{Eo}{(OhRe)^2} \int_{\Omega} \mathbf{g} \, dV \quad \text{in } \Omega_d, \end{aligned} \tag{7}$$

where V is the volume of Ω , dA is the area of Γ , and \mathbf{n} is the outward unit vector normal to the surface Γ .

In this study, it is assumed that the convection and diffusion of the mass dissolved from the dispersed phase exists only in the continuous phase. Therefore, the mass transfer expressed by the below equation is only considered in the cells in the continuous phase.

$$\int_{\Omega} \frac{\partial C}{\partial t} dV + \int_{\Gamma} C(\mathbf{u} - \mathbf{v}) \cdot \mathbf{n} dA = \frac{1}{ReSc} \int_{\Gamma} \mathbf{n} \cdot \nabla C dA \quad \text{in } \Omega_c, \quad (8)$$

where Sc is the Schmidt number and C is the concentration of the dispersed-phase mass in the continuous phase. For simplicity, the density of the continuous phase is not affected by the mass dissolved from the dispersed phase. Therefore, the mass in the continuous phase is passive to the flow field.

2.2. Numerical procedure

In the present method, a MAC-type projection scheme is adopted for solving the system of time-evolutionary equations. The NS equation is split into the following two steps:

$$\frac{\hat{\mathbf{u}} - \mathbf{u}^n}{\Delta t} = \text{CONV} + \text{DIFF} + \text{BUOY}, \quad (9)$$

$$\frac{\mathbf{u}^{n+1} - \hat{\mathbf{u}}}{\Delta t} = -\nabla \phi^{n+1}, \quad (10)$$

where CONV is the convection term, DIFF is the diffusion term, BUOY is the buoyancy term, $\hat{\mathbf{u}}$ is the intermediate velocity, and the superscripts n and $n + 1$ denote the computational time steps. Here velocity–pressure simultaneous iteration is adopted.

$$\frac{\mathbf{u}^m - \hat{\mathbf{u}}}{\Delta t} = -\nabla \phi^m, \quad (11)$$

where superscript m denotes the iteration number. By taking the divergence of Eq. (11), the Poisson equation for pressure is obtained

$$\frac{\nabla \cdot \hat{\mathbf{u}}}{\Delta t} = \nabla^2 \phi^m. \quad (12)$$

Integration in each computational cell gives

$$\frac{1}{V} \int_F (\nabla \cdot \hat{\mathbf{u}} - \Delta t \nabla \phi^m) \cdot \mathbf{n} dA = \frac{1}{V} \sum_F \text{FLUX}_F = 0, \quad (13)$$

where FLUX_F is the mass flux and the subscript F denotes the values on each cell face. Flux correction is carried out iteratively until incompressibility is attained. The residual, RES, of Eq. (13) is evaluated by

$$\text{RES} = \frac{\omega}{\Delta t \times \Delta^{-2}} \sum_F \text{FLUX}_F, \quad (14)$$

where Δ represents the cell size and ω is the relaxation parameter. When RES is smaller than a convergence criterion after several iterations, the obtained values at the m th iteration becomes the ones at the next time step. This procedure is continued in time-marching way.

2.3. Spatial discretisation

The present unstructured mesh system consists of triangular prisms near the interface for the sufficient resolution of boundary layers and of tetrahedrons in the other part, just like the ones used in Parthasarathy and Kallinderis [23]. For the spatial discretisation of the governing equations, a cell-centred finite volume

formulation on hybrid unstructured mesh is applied, following the Rhie–Chow’s algorithm [22], the essence of which appears in the discretisation of the convection term:

$$\int_F \mathbf{u}\mathbf{u} \cdot \mathbf{n} \, dA = \sum_F (\mathbf{u}_F \times \text{FLUX}_F), \tag{15}$$

where FLUX_F is the same as the one computed by Eq. (13), which gives stable computation of incompressible flow in collocated cell-centred grids. To calculate the surface integral in Eq. (15), \mathbf{u} on the cell face, \mathbf{u}_F , is required. In this study, the cell face values are obtained by using the Taylor series expansion

$$\mathbf{u}_F = \mathbf{u}_P + (\nabla\mathbf{u})_F \cdot \mathbf{r}_{PF} + \mathcal{O}(\mathbf{r}_{PF}^2), \tag{16}$$

$$(\nabla\mathbf{u})_F = \frac{1 + \lambda}{2} (\nabla\mathbf{u})_P + \frac{1 - \lambda}{2} (\nabla\mathbf{u})_N, \tag{17}$$

where λ is set to be $2/3$ to achieve upwinding third-order accuracy, rigorously in regular grids. The subscripts, P and N , denote the values at the centre of the concerned cell and at the centre of a neighbouring cell upon the concerned cell face, respectively. \mathbf{r}_{PF} is the distance vector from the centre of the concerned cell, P , to the area-centre of a cell face, F . Fig. 1 schematises this in the case of two-dimensional triangles. In Eq. (17), velocity gradients on each cell face are obtained by:

$$(\nabla\mathbf{u})_{P,N} = \frac{1}{V} \int_{\Gamma_{P,N}} \bar{\mathbf{u}}_F \cdot \mathbf{n} \, dA, \tag{18}$$

$$\bar{\mathbf{u}}_F = \frac{V_N \mathbf{u}_P + V_P \mathbf{u}_N}{V_N + V_P}. \tag{19}$$

This scheme is similar to the flux-vector-splitting of Batina [24], which was validated by comparing well with the measurement for the compressible flow over an airfoil.

Since the diffusion term consists of second derivatives, the calculation of first derivatives at cell faces is required in the cell-centred finite volume formulation. We use a local coordinate system, ξ_k ($k = 1, 2, 3$), at each cell face to compute the first derivatives

$$\frac{\partial u_j}{\partial x_i} = \frac{\partial \xi_k}{\partial x_i} \frac{\partial u_j}{\partial \xi_k} = J^{-1} b_{ik} \frac{\partial u_j}{\partial \xi_k}, \tag{20}$$

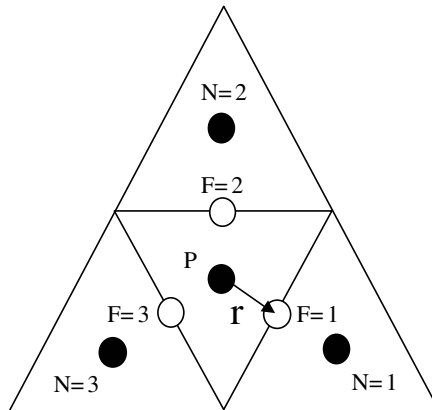


Fig. 1. Schematic sketch of neighbouring cells and a position vector from a cell centre to a cell face.

where ξ_1 is the direction connecting two cell-centres, and ξ_2 and ξ_3 are the ones between two diagonal nodes on the cell face, as are shown in Fig. 2. J and b_{ik} are the Jacobian and the contravariant metric tensor, respectively, of the coordinate transformation.

Velocities on nodes, which are required when calculating the gradients along ξ_2 and ξ_3 in Eq. (20), are obtained by using the single inverse-distance weighting average of the ones at the centres of the surrounding cells:

$$\mathbf{u}_X = \frac{\sum_N w_N \mathbf{u}_N}{\sum_N w_N}, \tag{21}$$

$$w_N = \frac{1}{|\mathbf{r}_{XN}|}, \tag{22}$$

where the subscript X refers to the value on a target node and \mathbf{r}_{XN} is the distance vector from the concerned node to the centre of the neighbouring cells. It is noted that this procedure is compatible to the way expressed by Eq. (19). This scheme for the diffusion term gives second-order accuracy in regular grids. This is also used for calculating second-derivative terms in the mass transfer equation and the Poisson equation for pressure, Eq. (13).

2.4. Time discretisation

Semi-implicit time integration is used both for the momentum and the mass transfer equations (6)–(8)

$$\begin{aligned} [(1/\Delta t)I + \beta(\text{CONV}_P - \text{DIFF}_P)]\mathbf{q}_P^{n+1} = &[-(1 - \beta)\text{CONV}_P + (1 - \beta)\text{DIFF}_P]\mathbf{q}_P \\ &+ [-\text{CONV}_X + \text{DIFF}_X]\mathbf{q}_X, \end{aligned} \tag{23}$$

where \mathbf{q} is a variable vector, I is the unit matrix, and β is an indicator for implicit time integration for cell-centred values. It is explicit when $\beta = 0$ and implicit in the other cases. The second term on the RHS indicates the portions that are computed from nodal values and this is always explicitly computed, whatever β is, so that it is called “semi”-implicit even if $\beta \neq 0$. This linear equation is solved by the Jacobi iteration at each time step of the computation.

Since all the evolutionary equations are decoupled explicitly and each one is solved implicitly ($\beta = 1$) with respect to time for the cell-centred values and explicitly for those on node points, the computation is not unconditionally stable. For an explicit method, the time increment between two time steps is limited by the Courant–Friedrichs–Lewy (CFL) condition, as is shown below:

$$\Delta t \leq \frac{c_1}{\frac{1}{V} \sum_F \bar{\mathbf{u}}_F \cdot \mathbf{n}A_F}, \tag{24}$$

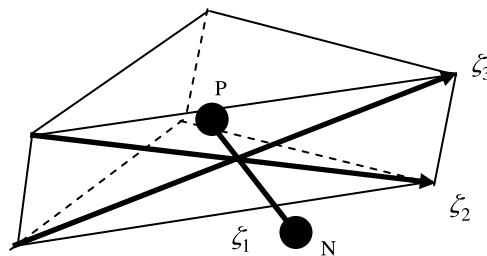


Fig. 2. Schematic sketch of the local coordinates on a cell-face to calculate first derivatives.

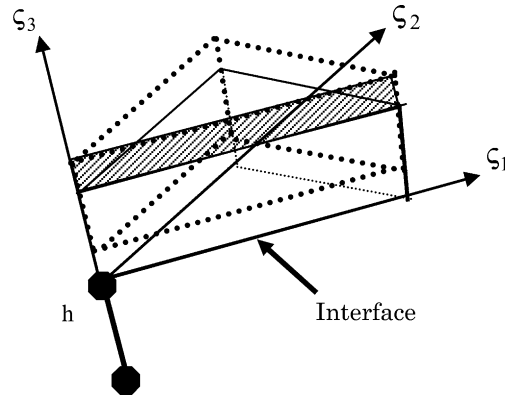


Fig. 3. Schematic sketch of the local coordinates of an interface cell. ζ_3 coincides with the direction of the spine, which represents the kinematic condition of the moving interface.

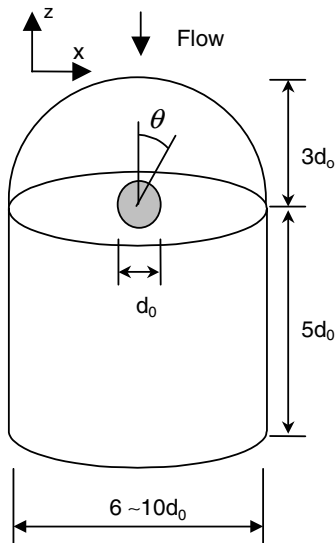


Fig. 4. Schematic sketch of the computational domain for flow over a droplet/solid sphere.

$$\Delta t \leq \frac{c_2}{2 \frac{2}{Re} \frac{1}{V^2} \sum_F A_F^2}, \frac{c_2}{2 \frac{2}{Re} \frac{\theta}{\gamma} \frac{1}{V^2} \sum_F A_F^2}, \tag{25}$$

where c_1 and c_2 are the Courant and the diffusion numbers, respectively. Because the present method is semi-implicit, it is not necessarily to follow the CFL condition and c_1 and c_2 can be more than unity. In this study, they were eventually set at 2.0 after checking computational stability.

2.5. Boundary conditions

The continuities of velocity and stress with the interface tension are imposed as the boundary conditions on the interface:

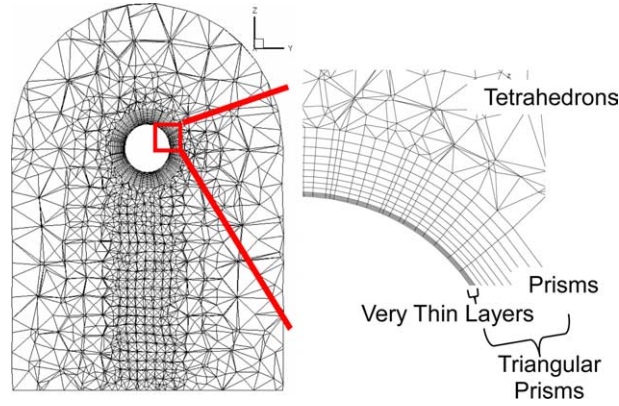


Fig. 5. A typical mesh system that shows the prism layers and the VTLs.

$$\mathbf{u}|_c = \mathbf{u}|_d, \quad (26)$$

$$-\phi|_c + \frac{2}{Re} \frac{\partial u_n}{\partial n}|_c = -\phi|_d + \frac{\kappa}{(OhRe)^2} + \frac{2\theta}{Re} \frac{\partial u_n}{\partial n}|_d, \quad (27)$$

$$\left(\frac{\partial u_n}{\partial s} + \frac{\partial u_s}{\partial n} \right)|_c = \theta \left(\frac{\partial u_n}{\partial s} + \frac{\partial u_s}{\partial n} \right)|_d \quad (28)$$

where κ is the interface curvature and $Q|_c$ and $Q|_d$ are any variable Q defined at the interface on the sides of the continuous and the dispersed phases, respectively. The direction indicators, n and s , denote the normal and the tangential components, respectively. The jump condition for pressure on the interface due to the existence of interface tension is given by Eq. (27), which is used in the Poisson solver for pressure. The tangential stress condition, Eq. (28), is used when calculating the diffusion terms in Eqs. (6) and (7) and, eventually, the dynamic condition of the interface is satisfied. Here the tangential gradient of the surface tension is not considered, in other words, the Marangoni effect is ignored, because it is assumed that the substance of the dispersed phase directly dissolves into the continuous phase in the present isothermal liquid–liquid system.

In this study, the dimensionless curvature κ is computed at triangle faces of the prism cells on the interface:

$$\kappa = \nabla \cdot \mathbf{n} = \frac{1}{A} \int \mathbf{n}_E \cdot d\mathbf{l}, \quad (29)$$

where \mathbf{n}_E is the unit normal vector to the interface on the edge and $d\mathbf{l}$ is the outward vector normal to the edge on the face plane, the value of which is the length of the edge, and A is the area of the triangle. We considered two ways in computing \mathbf{n}_E : the first way is the area-average of the unit normal vectors on the two neighbouring triangle faces upon the concerned edge. In the second way, the unit normal vectors at a node, \mathbf{n}_X , is calculated by taking the area-average of those of all the surrounding triangle faces. Then, the common average of the vectors at the both ends of the concerned edge gives \mathbf{n}_E . The second method is regarded as one more averaging than that in the first and, therefore, should give more smoothed curvature and is adopted in the present study. This was evidenced by a simple test for the unit sphere, the curvature of which is 4.0. The number of the generated triangle cells on the sphere is 590. Since the mesh on the

spherical surface is not completely smooth by the commercial mesh generator we used, the mean curvature by the first method is 4.035 and its standard deviation is 0.198, while by the second the mean and its standard deviation are 3.988 and 0.054, respectively.

For velocities, the uniform flow, the value of which is equal to the rise velocity of a droplet, is given at the inflow and the zero-gradient Neumann condition is set at the outflow, assuming that these outer boundaries are far enough from the droplet and the flow disturbances from the droplet are well diffused numerically there. The no-slip condition is applied to the surface of the wall in the case of a solid sphere. For pressure, the zero-gradient Neumann condition is applied to the outer boundaries. The standard pressure, 0.0, is given at some cells near the inflow.

The solubility of the dispersed phase in the continuous phase is given as the boundary condition for C on the interface when solving Eq. (8).

3. Treatment for high Schmidt number flow

3.1. Very thin layers

For high Schmidt number problems, the boundary layer for mass concentration is much thinner than that of momentum. According to a textbook [25], the thickness of mass boundary layer for flow over a flat plate can be expressed by a function of the Schmidt number and of the thickness of the momentum boundary layer:

$$\delta_c = \frac{\delta_M}{1.026Sc^{1/3}}, \quad (30)$$

$$\delta_M = \frac{5.48}{\sqrt{Re_L}} \frac{L}{2}, \quad (31)$$

where δ_c and δ_M are the thicknesses of mass and momentum boundary layers, respectively, and Re_L is the Reynolds number based on characteristic length L , which is set at d_0 in this study.

Based on the above empirical forms, the total thickness of prism layers and the thickness of the first prism to the interface are set at δ_M and δ_c , respectively. In order to resolve the thin mass boundary layer, we divided one prism layer attached to the interface into VTLs. It should be noted that the VTLs are used only for solving the mass transfer equation (8), where the velocities in the VTLs are linearly interpolated.

Table 1

Two grid systems for the flow over a solid sphere at $Re = 50$ and $Sc = 2.5$ for checking grid convergence by the calculated drag coefficients and the Sherwood numbers

	Case I-1	Case I-2	Case I-3
Re		50	
Sc		2.5	
Diameter of Domain	6	6	10
Tetrahedrons	14,201	24,778	44,406
Prisms (interface cell, layers)	5900 (590 × 10)	9960 (996 × 10)	5900 (590 × 10)
Cd (cal.)	1.63	1.64	1.64
Sh (cal.)	7.96	7.95	7.96

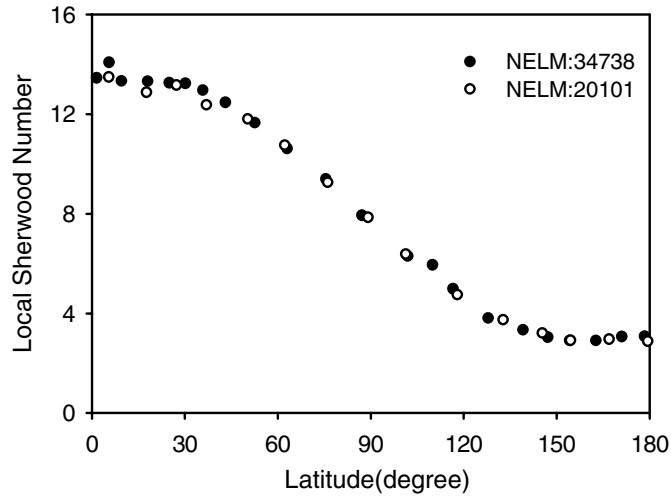


Fig. 6. Calculated local Sherwood number integrated at every latitude of a sphere by using two different mesh systems. The Reynolds and the Schmidt numbers are 50 and 2.5, respectively.

Table 2

Conditions of simulation for flow over a solid sphere and the calculated drag coefficients

	Case II-1	Case II-2	Case II-3	Case II-4
Re	50	100	500	1000
Diameter of domain	6	6	6	6
Tetrahedrons	14,201	14,201	24,778	60,291
Prisms (interface cell, layers)	5900 (590 × 10)	5900 (590 × 10)	9960 (996 × 10)	9960 (996 × 10)
C_d (cal.)	1.63	1.15	0.61	0.53

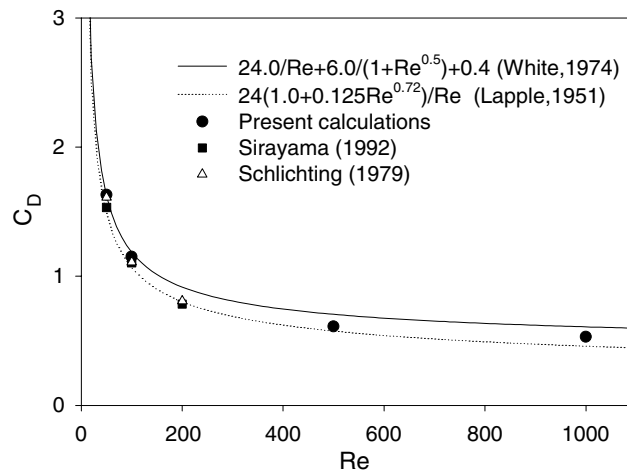


Fig. 7. Calculated drag coefficient of a solid sphere versus Reynolds number. Superimposed are the two empirical equations cited in Clift et al. [27] and the measurement by Schlichting [28], and the calculation by Shirayama [29].

3.2. Time integral for mass transfer

Since the VTLs are finer than the original prisms for the momentum solver, the time increment used in solving mass transfer becomes smaller than that for the momentum in the present semi-implicit scheme. Eventually, within one time step of the momentum solver, the mass transfer proceeds in several time steps. The time increments for the mass and momentum solvers, Δt_M and Δt_C , are determined by Eqs. (24) and (25), based on the respective mesh sizes, i.e., for the latter the thickness of the VTLs is considered. During the interval of Δt_M , only Eq. (8) is solved in a time-marching way by the increment of Δt_C , while the velocities remain the same.

4. Moving interface

Description of the moving interface follows:

$$\zeta_3 = h(\zeta_1, \zeta_2, t), \tag{32}$$

where ζ_i is the local coordinate vector, the direction of which is shown in Fig. 3, t is the time, and h is the spine function, which is a scalar representing the position of the interface, suggested by Mashayek and Ashgriz [26]. For a droplet in this study, h is the distance between a node on the interface and the gravity centre of the droplet. The kinematic condition of the moving interface is given by

$$\frac{\partial h}{\partial t} = U_3 - U_1 \frac{\partial h}{\partial \zeta_1} - U_2 \frac{\partial h}{\partial \zeta_2}, \tag{33}$$

$$U_i = \frac{\partial \zeta_j}{\partial x_i} u_j = J^{-1} b_{ij}^\zeta u_j, \tag{34}$$

where J is the Jacobian of metrics and b_{ij}^ζ is the contravariant metric tensor of the coordinate transformation. Only the prism layers generated near the interface deform according to the interface movement, i.e., the nodes at the interface move in the manner of Eq. (33) and, thereafter, the coordinate location of the rest nodes of the prism layers is distributed linearly.

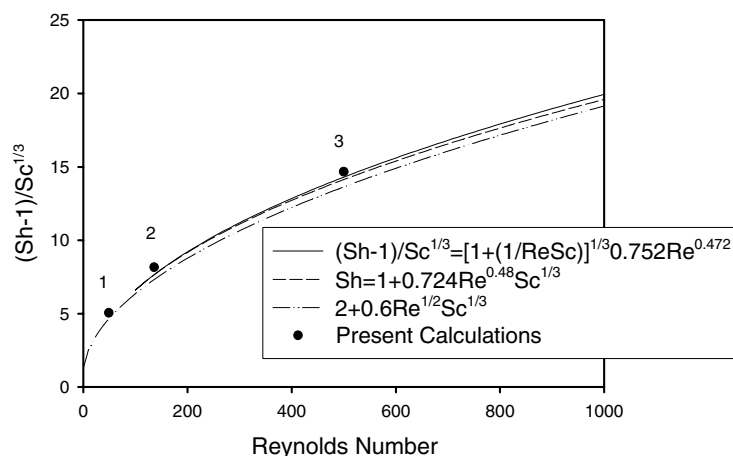


Fig. 8. Calculated Sherwood number in the form of a function of the Schmidt number versus the Reynolds number. Superimposed are two empirical equations cited in Clift et al. [27] and a classical one of Ranz and Marchall [30].

5. Results and discussions

5.1. Solid sphere in uniform flow

To verify the present numerical algorithm, numerical tests were performed for a flow over a solid sphere, from which a mass is dissolved into the continuous phase. The schematic view of the domain and an

Table 3

Conditions of simulation for flow over a solid sphere with mass dissolution from its interface

	Case III-1	Case III-2	Case III-3
Re	49	136	500
Sc	2.5	2.5	200
Diameter of domain	6	6	6
Tetrahedrons	14,201	14,201	32,925
Prisms (interface cell, layers)	5900 (590 × 10)	5900 (590 × 10)	15,940 (1594 × 10)
VTLs (interface cell, layers)	2950 (590 × 5)	2950 (590 × 5)	7970 (1594 × 5)
Sh (cal.)	7.86	12.07	20.90

The calculated Sherwood numbers are also listed.

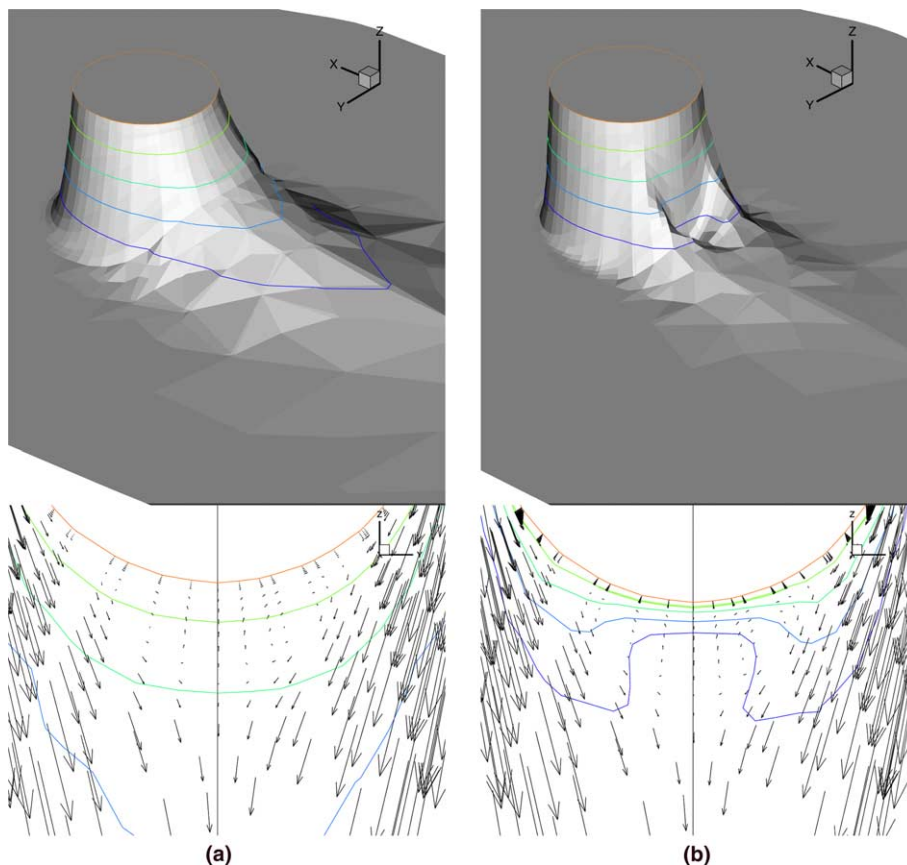


Fig. 9. Contour surfaces of mass concentration (upper) and velocity vectors (lower) on the plane sectioning the sphere centre at the same Reynolds number of 49, but at the different Schmidt numbers, 2.5 (a) and 50 (b).

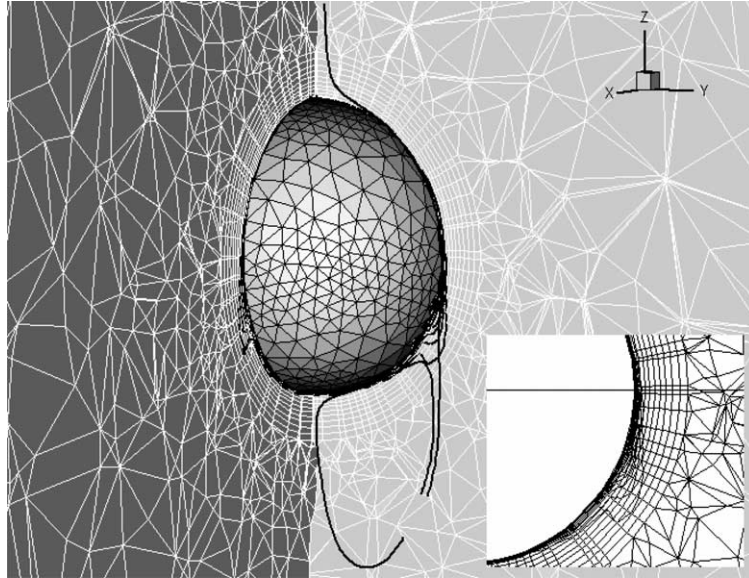


Fig. 10. Mesh system, the details of which are listed in Case II-3 in Table 2, for the flow over a solid sphere at the Reynolds and the Schmidt numbers of 500 and 200, respectively, visualised on two vertical planes and the sphere surface. A streamline and the contours of mass concentration are also shown.

Table 4
Conditions of simulation for flow over a rising silicon droplet in water

Re	826
Sc	2.5
Oh	0.0015
EO	2.82
γ	0.76
θ	0.494

example of the mesh system are shown in Figs. 4 and 5, respectively. In this solid sphere case, we neglect the buoyancy and, instead, the downward unflow of 1.0 comes into the domain from the upper boundary.

The mesh information is listed in Table 1, together with the calculated drag coefficients, C_D , and the calculated Sherwood number, Sh , at the dimensionless time of 4.36. The Reynolds and the Schmidt numbers are 50 and 2.5, respectively. It is noted that the differences in the drag coefficient and the Sherwood number using two mesh systems are less than 1%, comparing Cases I-1 and I-2. The calculated local point-wise Sherwood numbers on the latitudes of the sphere are plotted in Fig. 6 for both the mesh systems. They are in very good agreement. Therefore, it is believed that the grid convergence is attained at these particular Reynolds and the Schmidt numbers. Case I-3 is also considered for checking the domain size dependency in C_D for $Re = 50$. Since the result is almost the same as that in Cases I-1 and I-2, the computational domain with the diameter of $6d_0$ is thought to be wide enough.

Table 2 denotes the numbers of meshes used for the flows at the various Reynolds numbers. The calculated C_D are plotted in Fig. 7 with lines of the empirical equations cited by Clift et al. [27] and with data measured by Schlichting [28] and those calculated by Shirayama [29]. The present method gives almost the same results with them. The computational costs of the present method are, in Case II-4, 318 MB in

memory and 2.7 h per 1 dimensionless time by using CPU with the clock time of 980 MHz. Fig. 8 shows the calculated Sherwood numbers correlated with the Schmidt number at three sets of the Reynolds and the Schmidt numbers. The computational conditions are listed in Table 3. The solutions of two empirical equations cited in Clift et al. [27] and a classical one of Ranz and Marchall [30] are superimposed by solid, bro-


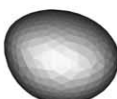

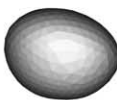

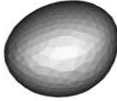

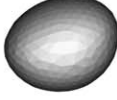


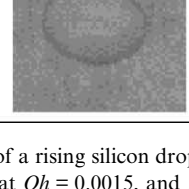

Measurement $Rn \approx 1300$	Period	Calculation $Rn \approx 1239$
	2T/9	
	4T/9	
	6T/9	
	7T/9	
	8T/9	
	T	

Fig. 11. Comparison of the shapes of a rising silicon droplet in water between the measurement (a) done by Imamura and Katayama [31] and the present calculation (b) at $Oh = 0.0015$, and $Eo = 2.82$. T_0 is a period of the sinusoidal trail of the droplet.

ken, and dash-dot-dotted lines, respectively. It seems that the results of the present calculation are in good agreement with these empirical equations. Judging from the results shown in Figs. 7 and 8, it is thought that the present numerical method and the way in determining the size of the prisms and the VTLs, described in Section 3.1, are validated at the wide range of the Reynolds and the Schmidt numbers.

Fig. 9 shows the contour surface maps and velocity vectors in the wake of the solid sphere on the central section of the sphere. The height of the contour surface indicates the mass concentration on the sectional plane. The Schmidt numbers are 2.5 and 50 for (a) and (b), respectively. The Reynolds number is 49 for both (a) and (b), so that the flow field is the same, because the computation of mass concentration is passive to the flow field in the present methods. Interestingly, the mass concentration fields in Fig. 9(a) and (b) are not similar, though the flow is the same. The contours are smooth in Fig. 9(a), where the mass diffusion is thought to be dominant rather than the flow convection at the lower Schmidt number. On the other hand, at the higher Schmidt number, the contours seem to match the flow field, in which the concentration is high, compared with the surroundings near the flow separation corresponding to the existence of a ring vortex, as is shown in Fig. 9(b).

The convection-dominant tendency in the mass distribution is more obvious as the Reynolds number becomes higher. Fig. 10 shows the mesh distribution and the contours of the mass concentration on two perpendicular vertical planes sectioning the sphere centre. An instantaneous streamline is also depicted in the figure. The Reynolds and the Schmidt numbers are 500 and 200, respectively (Case III-3 in Table 3). It is seen that the separation point locates at about 110° from the leading stagnation point and that the mass concentration is high just downstream of the separation.

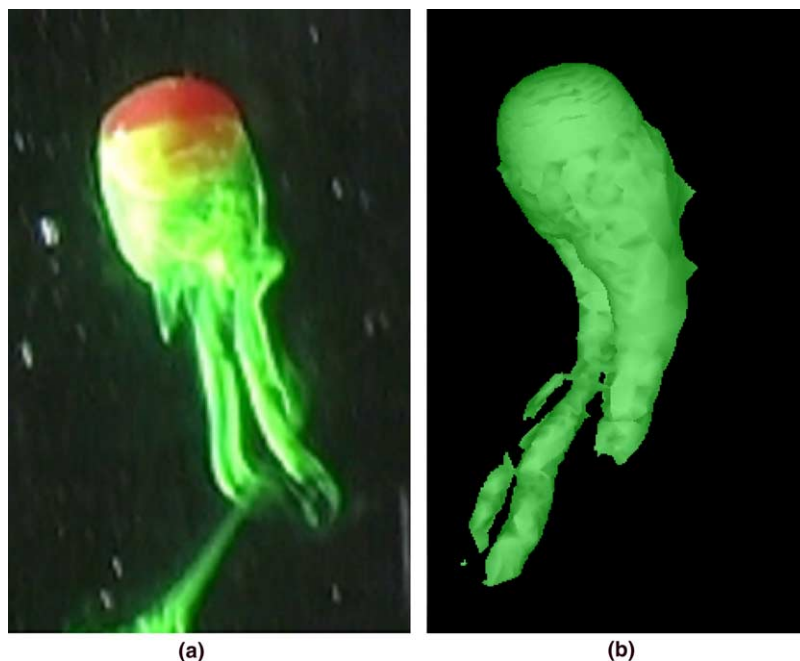


Fig. 12. Comparison of the wake structures of a rising silicon droplet in water between the measurement done by Katayama et al. [32] (a) and the present calculation (b). Sodium fluorescent is used for the visualisation of the hairpin and ring vortices in the measurement. The wake structure is visualised by an iso-surface of vorticity in (b) at $Rn \approx 1240$, $Oh = 0.0015$, and $EO = 2.82$.

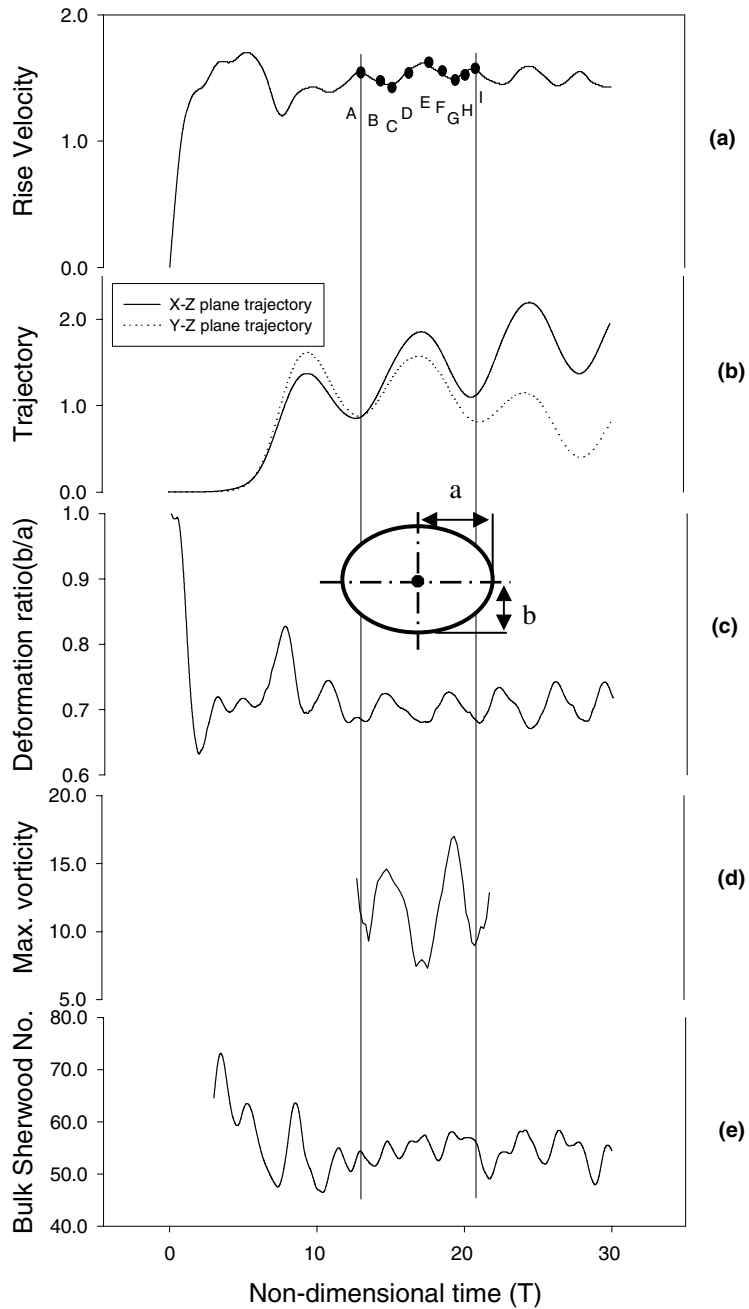


Fig. 13. Time histories of rise velocity (a), droplet trails in the vertical x - z and y - z planes (b), aspect ratio of the droplet (c), the maximum vorticity (d), and the Sherwood number (e) at $Rn \approx 1240$, $Sc = 2.5$, $Oh = 0.0015$, and $Eo = 2.82$. Two vertical guidelines are drawn at $T = 12.8$ and 20.4 , between which there is one period of the zigzag trail. Within the guidelines, nine specific timings are chosen for displaying flow structures, i.e., A, B, C, D, E, F, G, H, and I at $T = 12.8, 14.0, 15.0, 15.8, 17.2, 18.4, 19.2, 19.8,$ and 20.4 , respectively.

5.2. Rising droplet with mass transfer

Here a free rising silicon (KF-56, Shin-Etsu Chemical Co. Ltd.) droplet in water was simulated. The conditions of the simulation are listed in Table 4. This corresponds to the droplet diameter, d_0 , of 0.00826 m and the reference velocity, U , of 0.1 m/s. There are two kinds of the Reynolds numbers: i.e., $Re = (\rho_c U d_0) / \mu_c$ and $(Rn = \rho_c U_R d_0) / \mu_c$ based on the reference velocity, U , and the rise velocity of the droplet, U_R , respectively. In this study, the former and the latter are called the set and the rise Reynolds numbers, respectively. The volume of the droplet does not diminish by dissolution in this case.

The calculated changes in shape of the droplet with respect to time are compared with the experimental visualisation of Imamura et al. [31] in Fig. 11. The Reynolds number, Rn , based on the time-averaged rise velocity U_R of about $1.5U$ (as is shown later in Fig. 13(a)) is 1240 in the present calculations, while $Rn \approx 1300$ in the measurement. It is thought that the present method is quantitatively validated in this aspect. The calculated shape deformations are very similar to the measurement, although the eye directions in the experiment and in the calculation are not exactly the same. In Fig. 12, the calculated wake structure shown by an iso-surface of vorticity behind a rising droplet (b) is compared with the visualisation by means of sodium fluorescent dye done by Katayama et al. [32] (a). Although the dye distribution in the measurement and the vorticity contour in the calculation are different in visualising, ring and hairpin vortices are seen in the both figures and it is fair to say that the wake structure shown in Fig. 12(a) and (b) are qualitatively in good agreement.

Fig. 13 shows the time histories of the simulation results, such as the rise velocity (a), the vertical trails (b), deformation ratio (c), the maximum vorticity (d), and the Sherwood number (e) of the droplet. In addition, the horizontal trail is shown in Fig. 14, which shows a zigzag trail on a single vertical plane. In Fig. 13, two guidelines are drawn at $T = 12.8$ and 20.4 , between which there is one period of the zigzag trail. Within the guidelines, nine specific timings are chosen for displaying flow structures, i.e., A, B, C, D, E, F, G, H, and I at $T = 12.8, 14.0, 15.0, 15.8, 17.2, 18.4, 19.2, 19.8,$ and 20.4 , respectively. These timings are also plotted on the horizontal trail in Fig. 14. At the turning points (A, E, and I) of the trail, the rise velocity has the maxima and the aspect ratio has the minima. This may be because the droplet suffers large deformation due

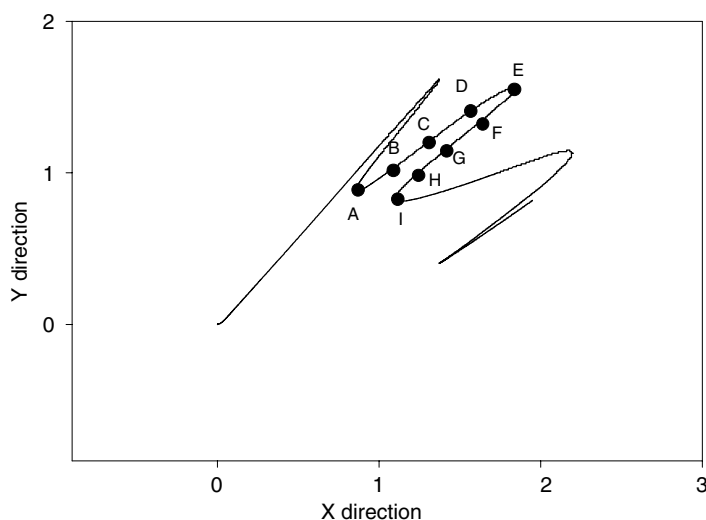


Fig. 14. Trail of a rising droplet on the horizontal (x - y) plane at $Rn \approx 1240$, $Oh = 0.0015$, and $Eo = 2.82$. The droplet starts at the origin $(0, 0)$. The alphabetic indicators are the same as those in Fig. 13.

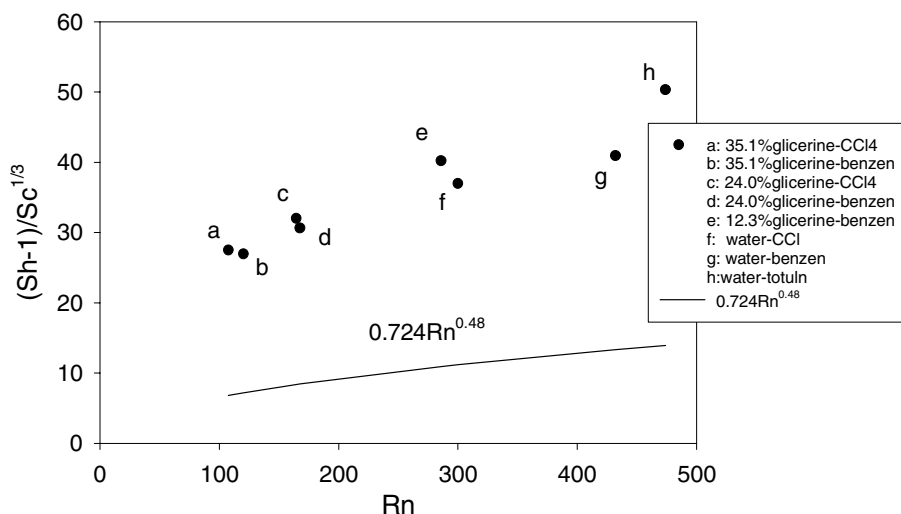


Fig. 16. Measured mass transfer rate in the form of a function of the Sherwood and the Schmidt numbers from droplets of the two-phase systems of glycerin- CCl_4 , glycerin-benzen, water- CCl_4 , water-benzen, and water-totuln, obtained by Yamaguchi et al. [33]. Superimposed by a solid line is an empirical equation for a solid sphere cited in Clift et al. [27].

Table 5

Conditions of simulation for flow over a rising droplet, corresponding to three different values of interface tension

	Case V-1	Case V-2	Case V-3
Re		250	
Sc		2.5	
Oh	0.0013	0.0020	0.0025
Eo	0.065	0.147	0.229
γ		0.76	
θ		0.494	

$$St = \frac{fd_0}{U}, \quad (36)$$

where St is the Strouhal number, f is the frequency of the shape oscillation, and $1 + \varepsilon$ is the ratio of maximum to minimum surface areas of the droplet that oscillates in shape. When the dimensionless numbers are the ones shown in Table 4 and the values read from Fig. 13(b) are $St \approx 0.92$ and $\varepsilon = 0.025$, Eq. (35) gives the Sherwood number of about 50, which is in good agreement with the numerical results shown in Fig. 13(e).

In order to see the relationship between the trail and the vortex shedding, the time variations of the contours of the vorticity component perpendicular to the x - y plane are depicted on the plane in Fig. 15. The drawing timings correspond to the position indicators, A to I, set in Figs. 13 and 14. It is seen that, when the droplet locates at the turning points, $T = 12.8$, 17.2 , and 20.4 , the ring vortex is shed from the droplet. At these moments, the rise velocity of the droplet increases rapidly and the droplet rises vertically, as are seen in Fig. 13. Fig. 15 also suggests that, on the way between two turning points, the ring vortex attached to the droplet is asymmetry. This may let us conjecture that the zigzag motion of the droplet is driven by the pressure unevenly distributed on the rear surface of the droplet. Considering that the zigzag trail is quite planar

on a single vertical plane, it is also inferred that the vortex shedding and the related uneven pressure distribution occur in a reciprocal way at the opposite sides on the rear surface of the droplet.

5.3. Effect of interface tension

It is expected that, when a droplet deforms in shape, the way of its rise and the rate of dissolution from it are different from those of a solid sphere. This was elucidated by Fig. 16, which shows a dimensionless function of the Sherwood and the Schmidt numbers versus the Reynolds number for a droplet of the two-phase systems of glycerin- CCl_4 , glycerin-benzen, water- CCl_4 , water-benzen, and water-totuln, based on the measurement done by Yamaguchi et al. [33]. A line is drawn based on an empirical equation cited in Clift et al. [27] for a solid sphere. It is obvious that the line is far from the measurements.

We simulated the three cases listed in Table 5, where the Ohnesorge and the Eötvös numbers vary depending on the change of the interface tension, with keeping the other dimensional parameters the same. The proper dimensionless number to discuss the effects of interface tension should be the Weber number ($We = Oh^2 Rn^2$), because droplet deformation is dominated by the inertia, which is resulted from the grav-

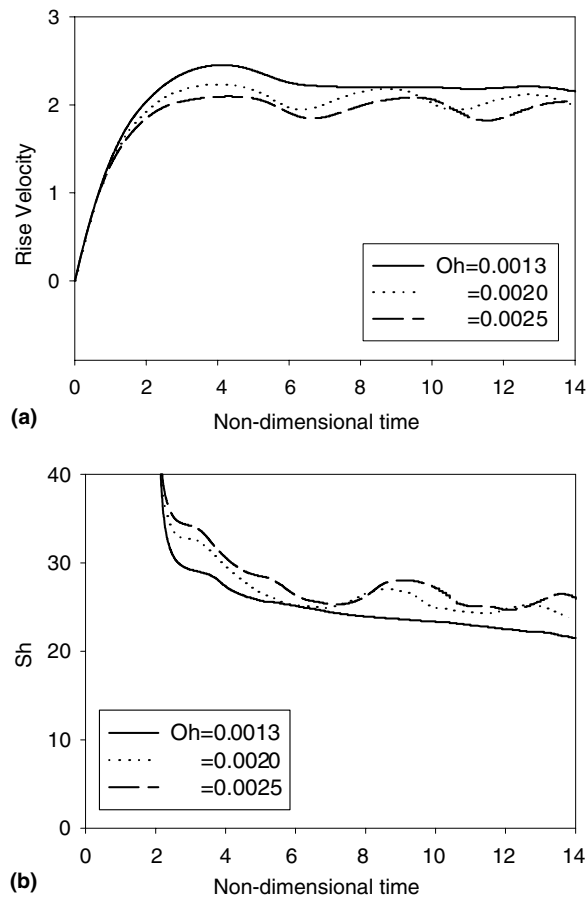


Fig. 17. Time histories of calculated rise velocity and Sherwood number at three different magnitudes of interface tension at almost the same Rn of about 500. The conditional parameters are listed in Table 5.

itational effect, as well as interface tension. However, the Weber number consists of Rn , which is based on the resultant rising velocity, and is not appropriate as a conditional parameter. Therefore, although Oh is used in the following discussions in this paper, it should be noted that Oh is only a representative of the interface tension and should be always set with other dimensionless parameters. In Fig. 17, the time histories of the dimensionless rise velocity and the Sherwood number are denoted. Under these conditions, the droplet deforms elliptically but does not oscillate distinctly. In Fig. 17(a), the time histories of the rise velocity at $Oh = 0.0020$ and 0.0025 oscillate, although that for the highest interface tension does not. It is known that the lower the interface tension, the more deformable the surface of the droplet is. As a result, the time histories of mass transfer rate at the interface in Fig. 17(b) also presents oscillations at $Oh = 0.0020$ and 0.0025 . Obviously, these oscillations in mass transfer rate are not because of shape oscillation but of the time change of rise velocity. It is also observed that the mass transfer rate is given in the opposite order of the magnitude of the interface tension.

Fig. 18 shows the dimensionless expression of mass transfer rate versus the Ohnesorge number that represents the interface tension. The error bars in the calculated data at $Oh = 0.0020$ and 0.0025 show the extrema of the dissolution rate with respect to time. A broken line is plotted based on an empirical equation of Clift et al. [27] for a solid sphere. It is thought that the difference of mean mass transfer rate becomes larger as the droplet deforms more. Clift et al. [27] cited the following correlation, obtained by solving boundary layer equations coupled with external irrotational flow, on the Sherwood number for a spherical droplet at $100 < Re < 1000$ and $\theta < 2$.

$$Sh = \frac{2}{\sqrt{\pi}} \sqrt{Sc Rn [1 - Rn^{-0.5} (2.89 + 2.15\theta^{0.64})]}, \tag{37}$$

where Rn is the rise Reynolds number. In the case that $Oh = 0.0025$, we can see that $U_R \approx 1.8U$ in Fig. 17(a) and this gives the Sherwood number of about 33. Although this is a little larger than the computed ones, the present computation is believed to give moderate dissolution rates, because Eq. (37) is applicable only to high Schmidt numbers and approximates empirical data that scatter very much.

In order to see the mechanism of the increase in mass transfer rate with respect to the interface tension, we selected three specific moments during the rise of the droplet, i.e., $T = 8.0, 9.0,$ and 10.0 . Fig. 19 shows

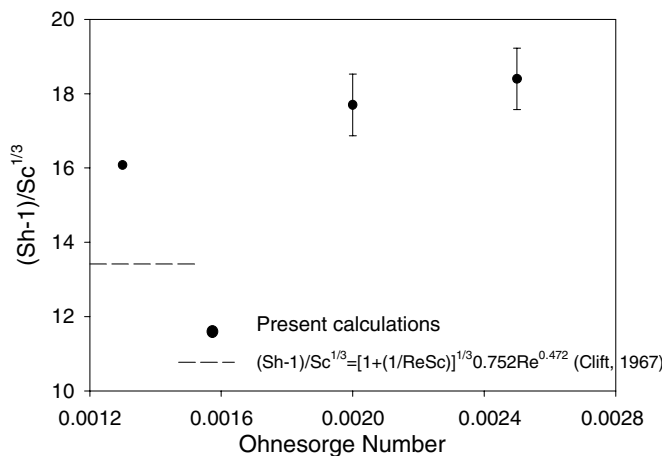


Fig. 18. Calculated mass transfer rate in the form of a function of the Sherwood and the Schmidt numbers. The conditional parameters are listed in Table 5. The error bars indicate the extrema caused by the deformation of a droplet. Superimposed by a broken line is an empirical equation for a solid sphere cited in [27].

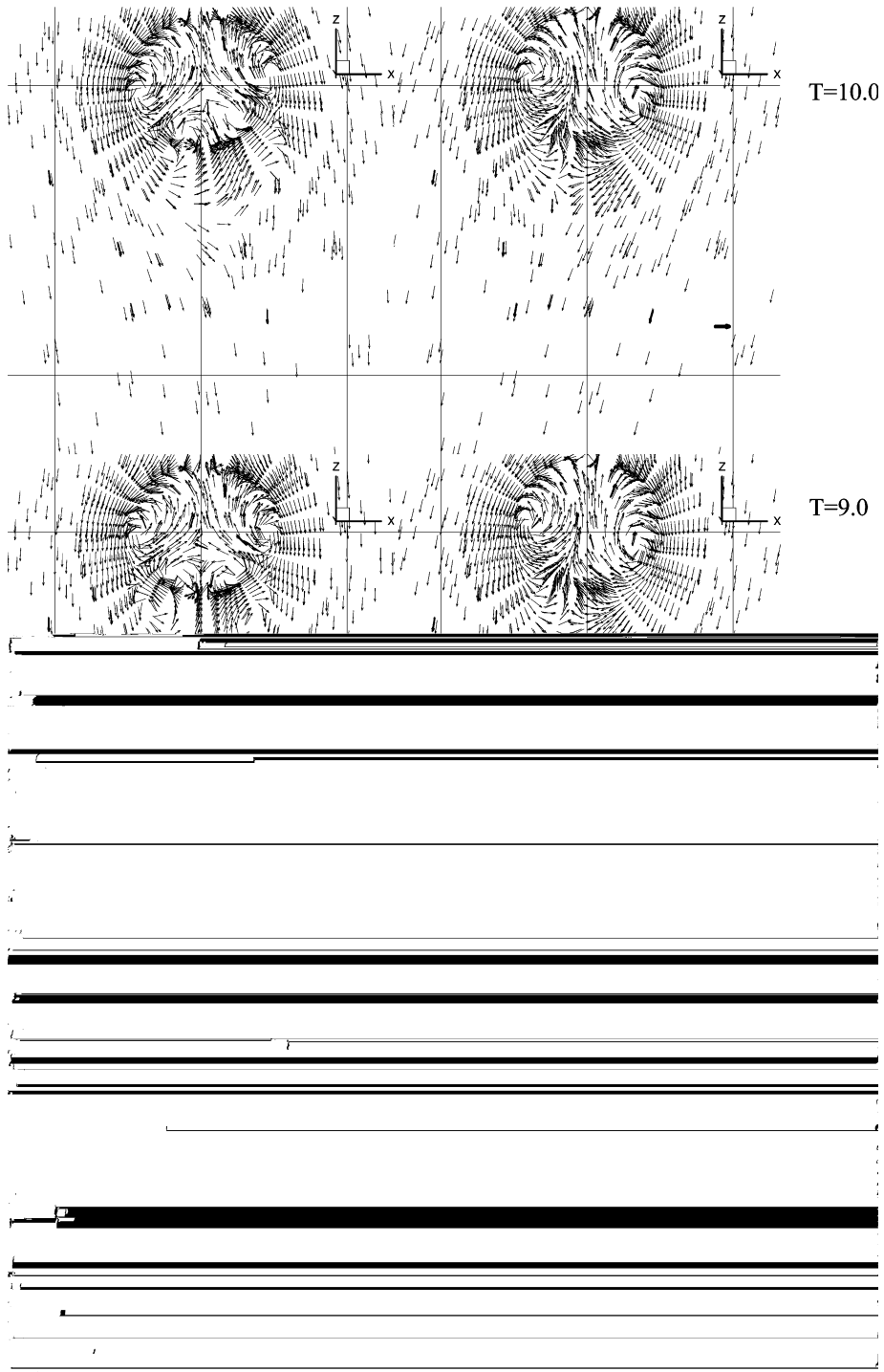


Fig. 19. Time variations of velocity vectors at $Oh = 0.0025$, $Eo = 0.229$ (a) and $Oh = 0.0013$, $Eo = 0.065$ (b) at $T = 8.0$, 9.0 , and 10.0 , at almost the same Rn of about 500.

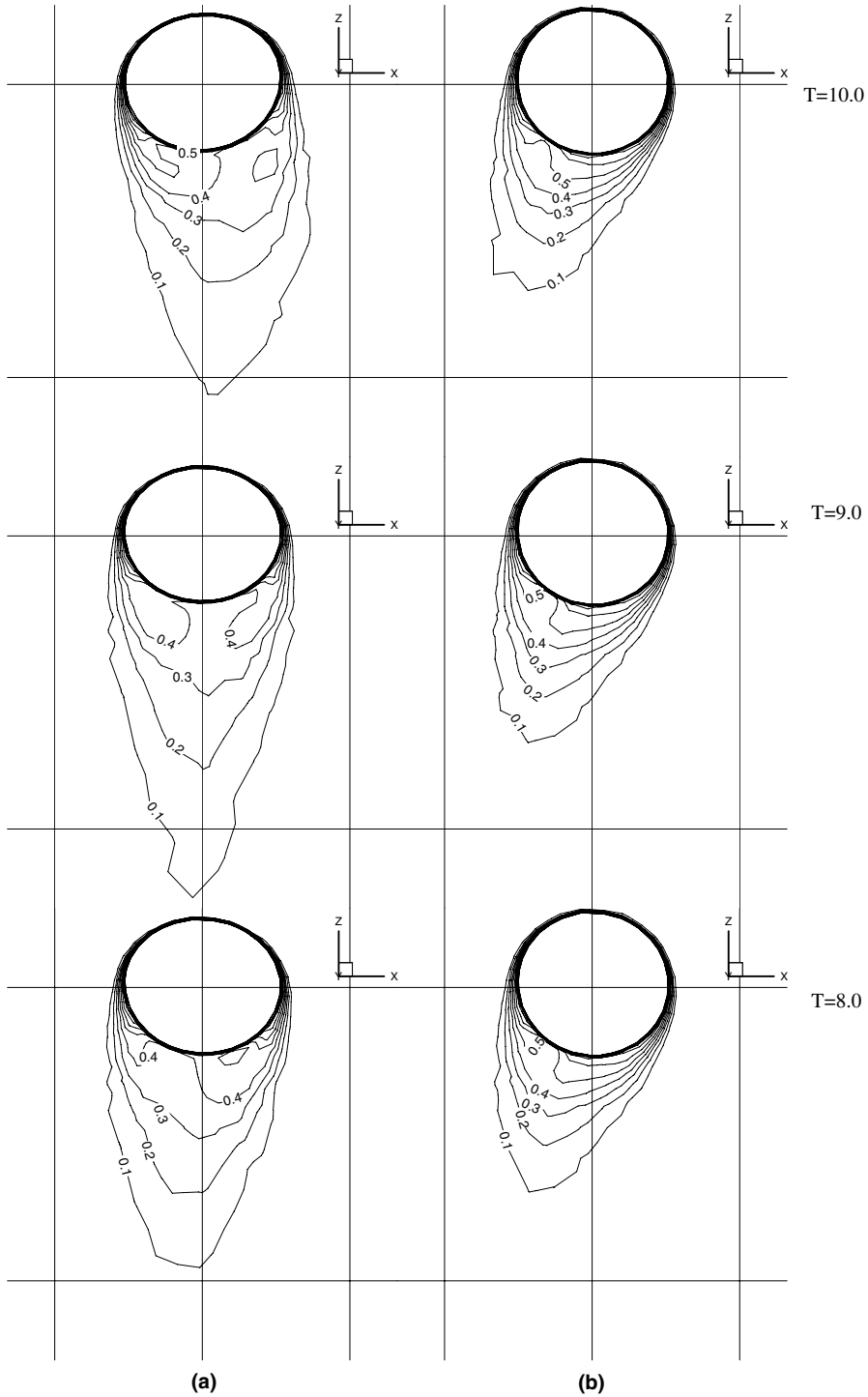


Fig. 20. Time variations of contour maps of dissolved mass in the continuous phase at $Oh = 0.0025$, $Eo = 0.229$ (a) and $Oh = 0.0013$, $Eo = 0.065$ (b) at $T = 8.0, 9.0$, and 10.0 , at almost the same Rn of about 500 and $Sc = 2.5$.

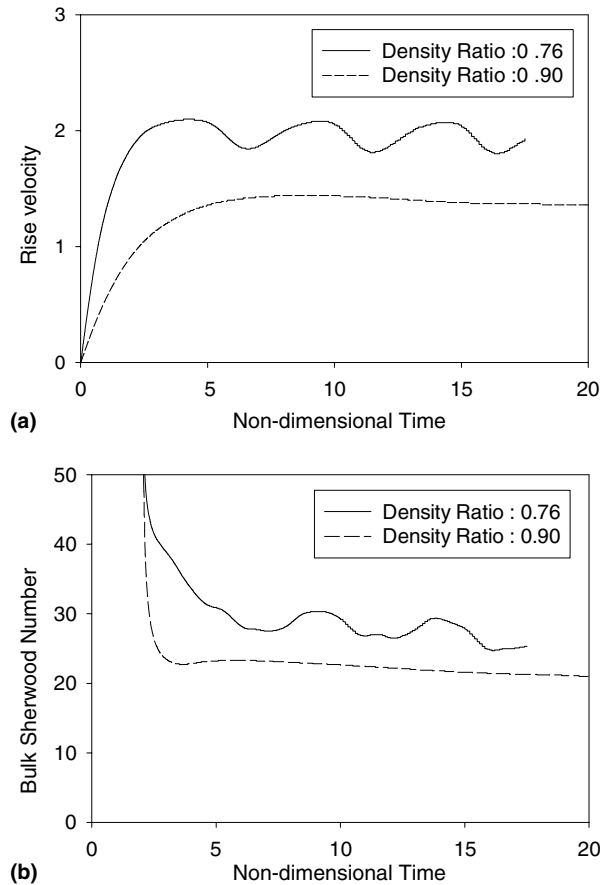


Fig. 21. Time histories of rise velocity (a) and bulk Sherwood number (b) for the density ratios of 0.76 (a) and 0.90 (b) at $Re = 250$, $Sc = 2.5$, $Oh = 0.0025$, $EO = 0.229$, and $\theta = 0.494$.

the time variations of velocity vector fields for $Oh = 0.0025$ and $Oh = 0.0013$. At almost the same rise Reynolds number of about 500, the velocity fields in the wake are drastically different depending on the deformation of the droplet. For the lower interface tension, the velocity vectors indicate a transient asymmetric ring vortex, while a steady weakly asymmetric vortex is attached to the droplet when the interface tension is high. Fig. 20 shows the time variations of the contours of the dissolved mass in the continuous phase. When the droplet shape is elliptic for the lower interface tension, the mass concentration on the rear surface is low at $T = 9.0$ than those at the other timings shown in Fig. 20(a). This may be due to the sweep of the high mass concentration by the shed vortices. This certainly accelerates the mass transfer rate near the separation. Therefore, it is thought that the vortex shedding caused by the droplet deformation for the lower interface tension gives rise to the higher Sherwood number than that for the higher interface tension, where we have no obvious shed vortices.

In Fig. 13, at the higher Reynolds number, the Sherwood number has half-period oscillations with respect to time compared with that of the rise velocity. This is different from the tendency shown in Fig. 17, where the frequencies of the oscillations of the rise velocity and the Sherwood number almost match. Both in Figs. 13 and 17, vortex shedding occurs in accordance with the oscillation of the rise velocity with

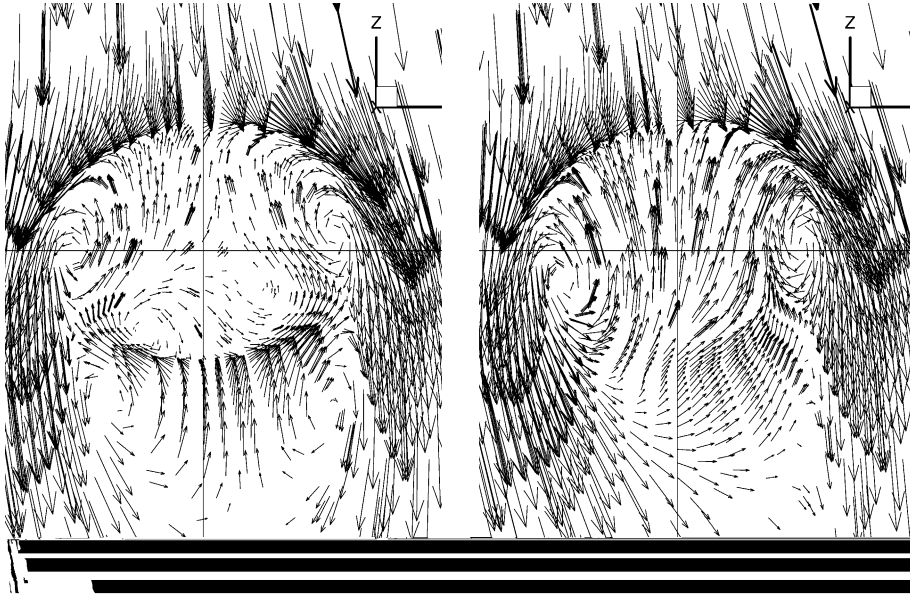


Fig. 22. Velocity vectors for the density ratios of 0.76 (a) and 0.90 (b) at $T = 14.5$ at $Re = 250$, $Oh = 0.0025$, $Eo = 0.229$, and $\theta = 0.494$.

respect to time. Therefore, there must be another mechanism for the higher Reynolds number flow for increasing the dissolution rate other than the vortex shedding. The notable difference between the droplet behaviour shown in Fig. 13 and that under the conditions of Cases V-2 and V-3 in Fig. 17 ($Oh = 0.0020$ and 0.0025) is that the former has the obvious shape oscillation with respect to time, not alone the deformation. It is recognised that, as well as the main frequency the same as that of the rise velocity, the deformation rate shown in Fig. 13(c) has another small oscillation, which has the frequency almost double of the main. Clift et al. [27] introduced the natural frequency of a droplet with spherical-oblate shape oscillation, as follows:

$$St_N = \frac{4}{\pi} \sqrt{\frac{3}{2 + 3\gamma} \frac{1}{Oh Re}}. \quad (38)$$

This gives the frequency of 0.86, which is close to the higher one, $St \approx 0.92$, shown in Fig. 13(c). Therefore, it is believed that the high frequency is due to the shape oscillation and the low main frequency is caused by vortex shedding, which also dominates the rise velocity oscillation with respect to time. In fact, the Sherwood number model shown by Eq. (35) for a droplet with shape oscillation is based on the idea that new mass is brought to the interface as its area increases and old mass is removed from the interface when the area decreases. This may explain the Sherwood number oscillation with time. Alternative interpretation can be given as follows. Since the dissolution on the rear surface is accelerated by the vortex shedding, the mass transfer rate on the leading side of the droplet may be responsible for the other oscillation. Because the maxima of the vorticity in Fig. 13(d) are given at the moment when the rise velocity is at the hollows in Fig. 13(a), the large shear rate may enhance the dissolution from the interface upper to the separation by refreshing the surrounding water. Further investigation is, however, necessary.

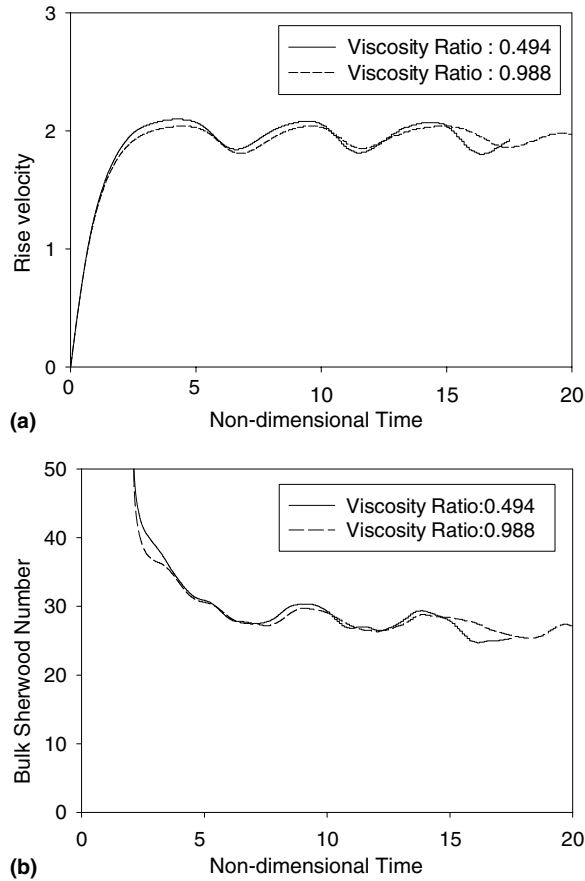


Fig. 23. Time histories of rise velocity (a) and bulk Sherwood number (b) for the viscosity ratios of 0.494 (a) and 0.988 (b) at $Re = 250$, $Sc = 2.5$, $Oh = 0.0025$, $Eo = 0.229$, and $\gamma = 0.76$.

5.4. Effect of density and viscosity ratios

The computational conditions to investigate the effect of different density ratio are based on Case V-3 in Table 5 by changing the density ratio, which has the values of 0.76 and 0.9. The time histories of the rise velocity and the Sherwood number are shown in Fig. 21. Because the density ratio is closely related to the rise velocity via buoyancy, this comparison simply gives differences due to the different rise Reynolds numbers, which are about 450 and 340 for $\gamma = 0.76$ and 0.9, respectively. The velocity vectors for the different density ratios at the dimensionless time of 14.5 are shown in Fig. 22. In Fig. 22(a), there is a ring vortex attached to the rear surface of the droplet in its wake and not in Fig. 22(b). At the same time, we can observe a circulation inside the droplet in both figures: the one in (a) locates upper than that in (b). In Fig. 22(a), it is seen that a secondary circulation at the inner bottom of the droplet, probably because of the existence of the ring vortex outside. Eq. (37) gives the Sherwood number of about 28 in the case of $\gamma = 0.9$, which is also larger than the value computed by the present method for the possible reason mentioned in Section 5.3. However, the ratio of this to that for $\gamma = 0.76$ is almost the same as that between the computed Sherwood numbers for $\gamma = 0.76$ and 0.9.

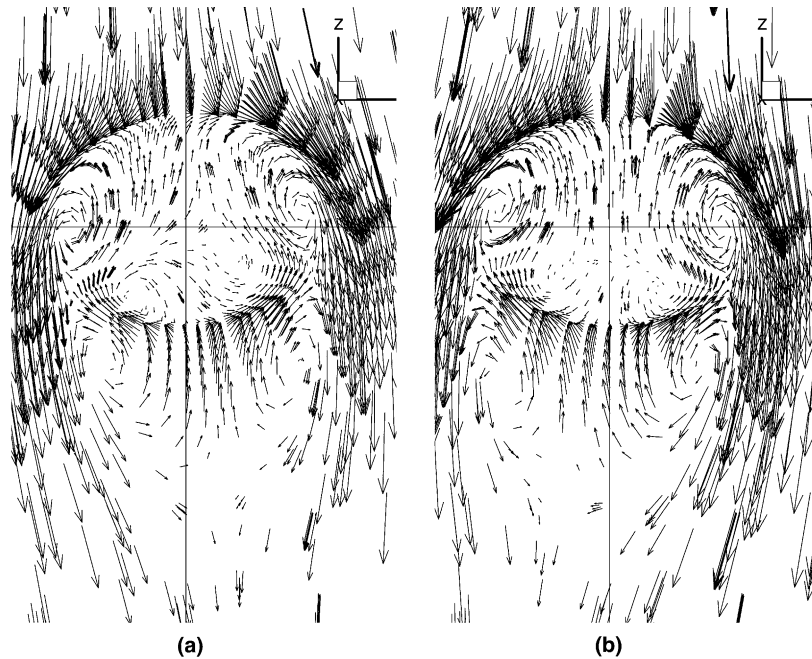


Fig. 24. Velocity vectors for the viscosity ratios of 0.494 (a) and 0.988 (b) at $T = 14.5$ at $Re = 250$, $Oh = 0.0025$, $EO = 0.229$, and $\gamma = 0.76$.

Next, we saw the effect of viscosity ratio. The computational conditions are, again, given by Case V-3 in Table 5 except for the viscosity ratios, 0.494 and 0.988. The time histories of the rise velocity and the Sherwood number are shown in Fig. 23. There seems to be no significant differences between the two values of the viscosity ratios both in the rise velocity and the Sherwood number. The velocity vectors for the different density ratios at the non-dimensional time of 14.5 are shown in Fig. 24. The velocity vectors also do not suggest main differences, except for the secondary circulations, which are slightly more distinctive in the case of lower viscosity ratio shown Fig. 24(a) than those in Fig. 24(b). Although the viscosity ratio is considered in Eq. (37), the discrepancy in the Sherwood number is not large between these cases and both give Sh of about 33 in significant digits. This does not contradict the discussion in this section.

6. Conclusions

A three-dimensional numerical code for two-phase flow, based on hybrid unstructured moving meshes, was developed. The newly developed technique in this study is the very-thin-layer cells, which are not used in computing flow field but in solving mass concentration, to resolve a thin mass boundary layer. For the momentum computation, explicit time integration is used, while the mass transfer solver adopts semi-implicit method with a smaller time increment than that for the former. We applied it to investigate the movement of a rising droplet in the continuous phase with mass dissolution from its interface.

The drag coefficient and the mass transfer rate of a solid sphere resulted from our numerical simulations are compared well with measurements and several empirical equations for checking the validity of the present method. Thereafter, we applied this method to the movement of the interface. The results indicate the correlation mechanism among the rise velocity, the zigzag trail, the shape deformation and oscillation of the

droplet, the vortex shedding from it, and mass transfer through the interface. We also investigated the effect of interface tension on the mass transfer rate and showed that the smaller the interface tension, the larger the dissolution from the droplet becomes.

Acknowledgement

Part of this work was financially supported by Research Institute of Innovative Technology for the Earth (RITE).

References

- [1] C.W. Hirt, B.D. Nichols, Volume of fluid (VOF) method for the dynamics of free boundaries, *J. Comput. Phys.* 39 (1981) 201.
- [2] A. Kanai, H. Miyata, Numerical simulation of bubbles in a boundary layer by Marker-Density-Function, in: *Proceedings of the 3rd International Conference on Multiphase Flow*, Lion, France, 1998.
- [3] M. Sussman, P. Smereka, S. Osher, A level set approach for computing solution to incompressible two-phase flow, *J. Comput. Phys.* 114 (1994) 146.
- [4] T. Sato, R.-T. Jung, S. Abe, Direct simulation of droplet flow with mass transfer at its interface, *J. Fluids Engng.* 122 (2000) 501.
- [5] E.G. Puckett, A.S. Almgren, J.B. Bell, D.L. Marcus, W.J. Rider, High-order projection method for tracking fluid interfaces in variable density incompressible flow, *J. Comput. Phys.* 100 (1997) 269.
- [6] Y.C. Chang, T.Y. Hou, B. Merriman, S. Osher, A level set formulation of Eulerian interface capturing methods for incompressible fluid flows, *J. Comput. Phys.* 124 (1996) 449.
- [7] M. Sussman, E. Fatemi, P. Smereka, S. Osher, An improved level set method for incompressible two-phase flows, *Comput. Fluids* 27 (6) (1998) 663.
- [8] P.E. Raad, S. Chen, D.B. Johnson, The introduction of micro cells to treat pressure in free surface fluid flow problems, *J. Fluids Engng.* 117 (1995) 683.
- [9] O. Ubbink, R.I. Issa, A method for capturing sharp fluid interfaces on arbitrary meshes, *J. Comput. Phys.* 153 (1999) 26.
- [10] A. Tomiyama, Y. Nakahara, S. Abe, An interface tracking method based on volume tracking in embedded micro cells, in: *Proceedings of the ASME FEDSM2002*, 31147, Montreal, Canada, 2002.
- [11] F.H. Harlow, J.E. Welch, Numerical calculation of time-dependent viscous incompressible flow of fluid with free surface, *Phys. Fluids* 8 (1965) 2181.
- [12] S.O. Unverdi, G. Tryggvason, A front-tracking method for viscous incompressible multi-fluid flows, *J. Comput. Phys.* 100 (1992) 25.
- [13] G. Tryggvason, B. Bunner, A. Esmaeeli, S. Mortazavi, Direct numerical simulations of dispersed flows, in: *Proceedings of the 3rd International Conference on Multiphase Flow*, Lion, France, 1998.
- [14] G. Agresar, J.J. Linderman, G. Tryggvason, K.G. Powell, An adaptive, Cartesian, front-tracking method for the motion, deformation and adhesion of circulation cells, *J. Comput. Phys.* 143 (1998) 346.
- [15] T. Sato, S.M. Richardson, Numerical simulation method for viscoelastic flows with free surface – Fringe element generation method, *Int. J. Numer. Meth. Fluids* 19 (1994) 555.
- [16] D. Enright, R. Fedkiw, J. Ferziger, I. Mitchell, A hybrid particle level set method for improved interface capturing, *J. Comput. Phys.* 183 (2002) 83.
- [17] H. Miyata, T. Sato, N. Baba, Difference solution of a viscous flow with free-surface wave about an advancing ship, *J. Comput. Phys.* 72 (2) (1987) 393.
- [18] G.R. Ryskin, L.G. Leal, Numerical solution of free-boundary problems in fluid mechanics. Part 1. The finite-difference technique, *J. Fluid Mech.* 148 (1984) 1.
- [19] S. Takagi, Y. Matsumoto, H. Huang, Numerical analysis of a single rising bubble using boundary-fitted coordinate system, *JSME Int. J. Series B* 40 (1997) 42.
- [20] S. Popinet, S. Zaleski, A front-tracking algorithm for accurate representation of surface tension, *Int. J. Numer. Meth. Fluids* 30 (1997) 775.
- [21] H. Braess, P. Wriggers, Arbitrary Lagrangian–Eulerian finite element analysis of free surface flow, *Comput. Methods Appl. Mech. Engng.* 190 (2000) 95.
- [22] C.M. Rhie, W.L. Chow, Numerical study of the turbulent flow past an airfoil with trailing edge separation, *AIAA J.* 21 (11) (1983) 1525.

- [23] V. Parthasarathy, Y. Kallinderis, Adaptive prismatic-tetrahedral grid refinement and redistribution for viscous flows, *AIAA J.* 34 (4) (1996) 707.
- [24] J.T. Botina, Implicit flux-split Euler schemes for unsteady aerodynamic analysis involving unstructured dynamic meshes, *AIAA J.* 29 (11) (1991) 1836.
- [25] J.A. Schetz, *Boundary Layer Analysis*, Prentice-Hall, New York, 1993.
- [26] F. Mashayek, N. Ashgriz, A spine-flux method for simulating free surface flows, *J. Comput. Phys.* 122 (1995) 369.
- [27] R. Clift, J.R. Grace, M.E. Weber, *Bubbles, Drops and Particles*, Academic Press, New York, 1978.
- [28] H. Schlichting, *Boundary Layer Theory*, seventh ed., McGraw-Hill, New York, 1979, p. 17.
- [29] S. Shirayama, Flow past a sphere: Topological transitions of the vorticity field, *AIAA J.* 30 (1992) 349.
- [30] W. Ranz, W. Marshall, Evaporation from drops: Part I, *Chem. Engng. Prog.* 48 (1952) 141.
- [31] K. Imamura, T. Katayama, A study of droplet movement and dissolution in liquid–liquid two-phase flow, Graduation Thesis, Department Ocean Engineering, University of Tokyo, 1999 (in Japanese).
- [32] T. Katayama, K. Imamura, T. Sato, R.-T. Jung, Y. Tsuchiya, A study of movement of the liquid–liquid interface and mass transfer through it, *Trans. Vis. Soc. Jpn.* 21 (2) (2001) 45 (in Japanese).
- [33] M. Yamaguchi, T. Fujimoto, T. Katayama, Experimental studies of mass transfer rate in the dispersed phased and moving behavior for single oscillating drops in liquid–liquid systems, *J. Chem. Engng. Jpn.* 8 (5) (1975) 361.